International Journal of Geosciences, 2025, 16(11), 890-912
https://www.scirp.org/journal/ijg
ISSN Online: 2156-8367
ISSN Print: 2156-8359

Mineral Mapping and Mineralization Exploration of Epithermal Gold Deposit in Bijia Mountain, NW China, Using GF-5 and EMIT Data

Haoyang Qin, Shijie Li*, Haiyang He, Xiaoyu Liu, Xu Sun

Xi'an Center of Mineral Resources Survey, China Geological Survey, Xi'an, China
Email: *xkd_workteam@foxmail.com

How to cite this paper: Qin, H.Y., Li, S.J., He, H.Y., Liu, X.Y. and Sun, X. (2025) Mineral Mapping and Mineralization Exploration of Epithermal Gold Deposit in Bijia Mountain, NW China, Using GF-5 and EMIT Data. *International Journal of Geosciences*, **16**, 890-912.
https://doi.org/10.4236/ijg.2025.1611044

Received: September 26, 2025
Accepted: November 23, 2025
Published: November 26, 2025

Abstract

Spectral analysis technology can identify minerals and their compositions based on spectral absorption characteristics. With hyperspectral remote sensing data, alteration minerals mapping in the wild range could be used for mineral prospecting. However, whether hyperspectral data with low spatial resolution can be used in the exploration of small-scale deposits is worth discussing. The Bijia Mountain deposit is a small-scale epithermal gold deposit located in the Dahananhu island arc belt in northern China, which has great potential for porphyry and epithermal gold-copper deposit prospecting. The alteration minerals distribution on surface and core samples was analyzed with hyperspectral data (GF-5 and EMIT) and a spectrometer. The alteration minerals, as well as the composition of sericite and chlorite, were identified using a tool developed with Python programming based on the Tetracorder algorithm. The mapping result showed the alteration zones: advanced argillic alteration (alunite + pyrophyllite + kaolinite) in the core of the mine, argillic alteration (sericite + montmorillonite), and propylitization alteration (chlorite + calcite). The composition of sericite and chlorite and the connections between mineralization and alteration minerals were discussed with high-sulfur epithermal metallogenic theory in this paper.

Keywords

Mineral Mapping, GF-5, EMIT, Spectral Feature Extraction, Epithermal Gold Deposit

1. Introduction

Hydrothermal altered minerals were formed from the interaction between hydro-

*Corresponding author.

thermal fluid and host rocks in mineralization. The composition differences of some hydrothermal altered minerals caused by cation exchange can reflect the pH value, fluid-rock interaction process, and temperature of the ore-bearing hydrothermal solution. Therefore, altered minerals and alteration zone mapping could serve as effective indicators for prospecting of hydrothermal deposits [1] [2]. Spectral analysis technology can extract spectral diagnostic features caused by functional groups, including hydroxyl (OH^-), carbonate (CO_3^{2-}), and sulfate (SO_4^{2-}) in different altered minerals, and recognize the compositions and abundance of minerals based on the shift and depth of the diagnostic absorption features [3]. Some specific spectral parameters, such as the sericite 2200-nm absorption wavelength shift, chlorite 2250-nm absorption wavelength shift, as well as the illite and kaolinite crystallinity, were used to recognize the mineral composition and the ore-forming environment [4] [5]. According to the research on epithermal deposits, different alteration zones with various assemblages of alteration minerals could indicate the position and stages of mineralization [6]. As a typical metallogenic model of the high sulphur (HS) epithermal gold deposit, the ore-forming fluids migrate upward from the bottom, driven by a deep-seated thermal source, and interact with host rocks on the surface. Vertical-horizontal alteration zones are formed in this process, such as a propylitic zone dominated by chlorite and epidote; an advanced argillic zone composed of alunite, pyrophyllite, and kaolinite; sericitization dominated by sericite [7]. All of the above-mentioned alteration minerals have identifiable short-wave infrared (SWIR) spectral characteristics, which could become critical indicators for remote sensing mineral exploration [8]-[10].

Hyperspectral remote sensing images usually have hundreds of narrow spectral bands that cover the short-wave infrared (SWIR) wavelength range. Such high spectral resolution makes it possible to accurately identify and map alteration minerals and zones. Compared to extracting alteration anomalies from multispectral data such as ASTER and Sentinel-2A, hyperspectral images combined with spectral analysis technology could identify specific alteration minerals, and have become an efficient method for alteration zone and mineral mapping [11]-[13]. In studies from the last few years, hyperspectral remote sensing data with a 400 - 2500 nm wavelength range, such as Hyperion, AVIRIS, HYMAP, and CASI, have been widely used in geological prospecting and exploration in several countries [14]. Despite the significant discoveries of porphyry and epithermal hydrothermal alteration zones based on these data, the relatively small coverage area of airborne hyperspectral data and the high costs of data acquisition limit its application range. With the advancement of hyperspectral sensors, satellite hyperspectral data with larger coverage and easier acquisition have emerged in recent years, such as GF-5 of China launched in 2018, EMIT of the U.S. carried in 2022, and EnMap of Germany launched in 2022. There have been numerous studies in recent years that use these remote sensing data for mineral mapping and exploration, most of which focused on mineralization belts or large-scale deposits [15]-[17]. It is primarily due to the fact that, although satellite hyperspectral data have high data quality, signal-to-noise ratio (SNR), and

spectral resolution, the spatial resolution of these data is lower than 30 m, and whether they have sufficient detection capability to discover hydrothermal alteration traces in small and medium scale deposits remains an issue that is worth discussing.

The Bijia Mountain gold deposit, located in the Dananhu island arc belt in northwestern China, is a small-sized but high-grade epithermal gold deposit that contains about 4 tons of gold. The mining area has intensive alteration and well-exposed rocks, making it a vantage region for remote sensing mineral mapping. Owing to the absence of high-quality hyperspectral remote sensing data before, the deposit lacked studies based on hyperspectral remote sensing data and techniques, which limited the research on mineral distribution and alteration in the mining area.

This paper completed altered mineral identification and alteration zones mapping in the Bijia Mountain gold deposit with GF-5 and EMIT hyperspectral images, which have the best design parameters of sensors and data quality in the world. The core samples' spectrum was also studied using the spectrometer. The distribution of about 10 altered minerals with the composition of chlorite and sericite was identified, and the spatial distribution of mineralized alteration zones was mapped. This study suggests the capability of satellite hyperspectral remote sensing for mineral mapping and prospecting in small-scale hydrothermal deposits. The Dananhu island arc belt is an important polymetallic metallogenic belt containing multiple epithermal gold and copper deposits. The result provided effective remote sensing indicators and mapping methods that could guide mineral exploration in deposits with similar genesis types and geological backgrounds.

2. Geologic Setting

The island arc belt is a favorable location for the occurrence of epithermal deposits and porphyry deposits (**Figure 1**). The Dananhu island arc belt is located within the Turfan-Hami block, at the convergent boundary between the Junggar Plate and the Tarim Plate, with exposed strata ranging in age from the Ordovician to the Carboniferous [18]. The southern side of the Dananhu island arc hosts major faults such as the Yamansu-Kushui Fault and the Kangguer Fault. The exposed strata are predominantly composed of volcaniclastic rocks and intermediate-mafic volcanic rocks, with minor amounts of acidic volcanic rocks [19]. The mineralization in this region is mainly controlled by stratigraphy and faults. Many porphyry and epithermal Cu-Au deposits discovered within the island arc belt, such as Tuwu, Yandong, Chihu, and the Huangshan deposit, are distributed in an east-west trend near the Yamansu-Kushui fault. The ore-hosted strata are primarily Carboniferous tuff and andesite, with a few occurrences of intermediate-acidic lava in some deposits, reflecting a magmatic evolution sequence from mafic to intermediate and then to acidic volcanism in this region. Widespread alteration is observed in the ore-hosted strata: andesite commonly exhibits silicification and sericitization, while in tuff, crystalline fragments are frequently chloritized, and the volcanic ash matrix often shows kaolinization.

The Bijia Mountain gold deposit, which shares a similar metallogenic environment with other epithermal deposits and porphyry deposits in this region, is located within NW-trending secondary faults on the northern side of the Yamansu-Kushui major fault in the Dananhu island arc belt. The deposit developed intensive tectonic activities and alteration, making it one of the typical hydrothermal alteration gold deposits in the east Tianshan metallogenic belt. The exposed strata in the mining area were shown as late Carboniferous intermediate-acid volcanics and pyroclastic rocks accompanied by a few early Permian foliated granite (**Figure 2**). The granitoid intrusions that are associated with mineralization were mainly distributed in the southeastern and northeastern parts, and they were presented as cataclasite, phyllitization, and mylonitization along the fault strike. Most of the gold occurred in the late Carboniferous volcanic-sedimentary rocks, including tuff, andesite, and volcanic breccia.

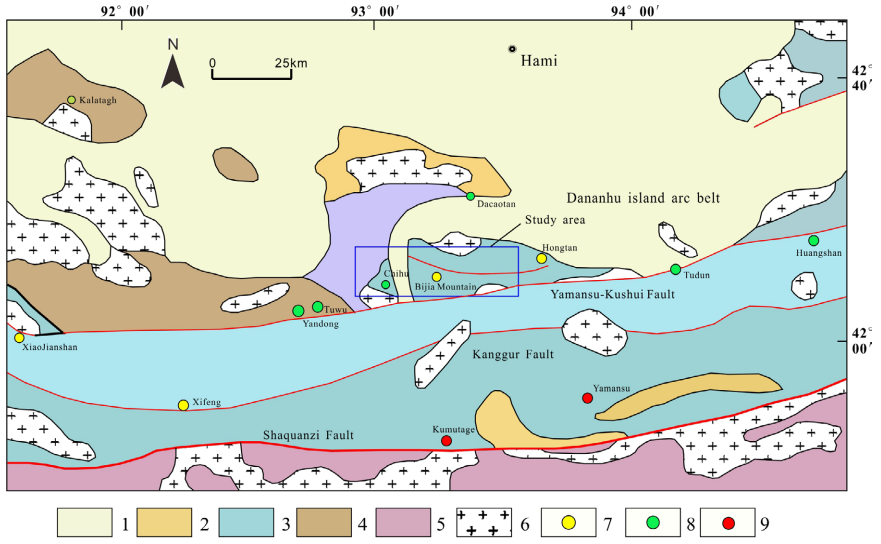

Figure 1. Regional geological map of the Dananhu island arc belt [20].

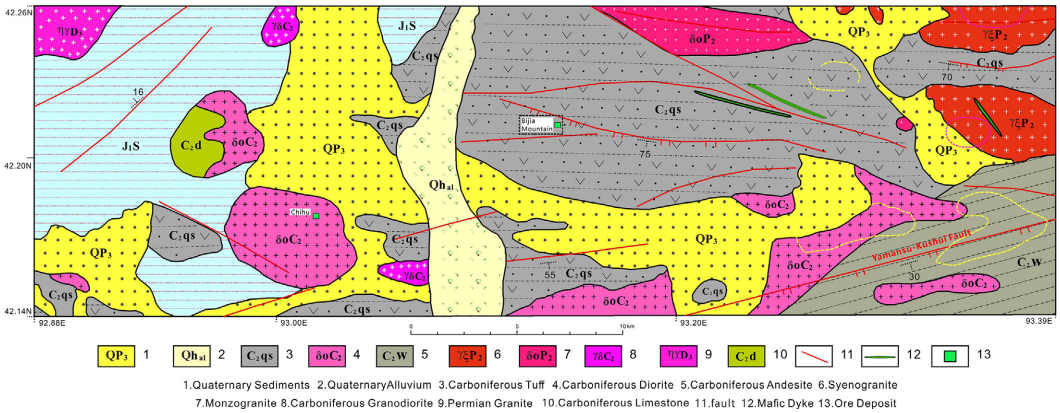

Figure 2. Geological map of the Bijia Mountain gold deposit.

The metallization of the Bijia Mountain deposit was controlled by the EW, NW 320˚ trending secondary faults and a set of meters-wide crisscross dikes. The deposit occurred in the fault fracture zone, filled with ore-bearing quartz vein, which contains limonite and pyrite. There was intense metallization alteration with altered minerals mainly including alunite, pyrophyllite, pyrite, quartz, sericite, and kaolinite in the rocks exposed at the surface (Figure 3).

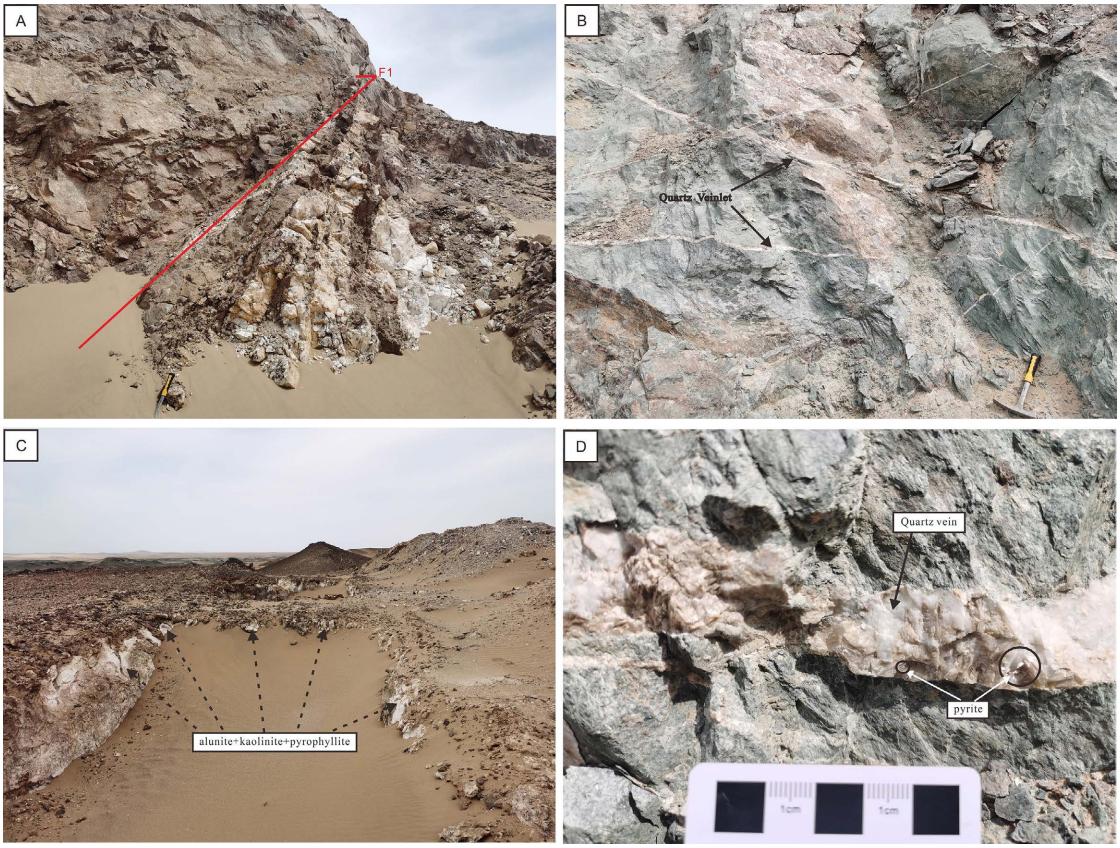

Figure 3. Photographs showing mineralization and alteration of the Bijia Mountain Au deposit. (A) Altered rock distributed along fault strike; (B) Quartz veinlets in tuff; (C) Advanced argillic alteration zone and altered minerals exposed at the surface; (D) Quartz vein with disseminated pyrite/limonite in tuff.

3. Materials and Methods

3.1. Hyperspectral Remote Sensing Data

This paper used GF-5 (Gaofen-5) and EMIT (Earth Surface Mineral Dust Source Investigation) remote sensing data for mineral mapping and compared the two sets of mapping results to ensure they were accurate and reliable.

The GF-5 (Gaofen-5) satellite, launched on May 9th, 2018, is a Chinese hyperspectral observation satellite that is equipped with hyperspectral and multispectral sensors, which allow it to capture detailed images and data across many narrow spectral bands. The VNIR signal-to-noise ratio (SNR) of AHSI data is nearly 700, whereas the SNR of SWIR can reach approximately 500.

The EMIT (Earth Surface Mineral Dust Source Investigation) remote sensor

that was carried by the International Space Station (ISS) on January 14th, 2022, is a hyperspectral sensor developed by the National Aeronautics and Space Administration (NASA). The EMIT provides L2A-level surface reflectance data with an extremely high signal-to-noise ratio and imaging quality. The parameters of the two satellites are listed in Table 1.

In this paper, we collected GF5-AHSI data acquired on January 28th, 2019, and EMIT data acquired on February 4th, 2023, for mineral mapping. Both of the images are clear with less than 5 percent cloud cover. The GF-5 AHSI data were obtained from the GeoCloud online platform (https://geocloud.cgs.gov.cn/), and the EMIT data were obtained from the NASA Earthdata.

Table 1. Parameters of Gf-5 and EMIT hyperspectral data.

Hyperspectral Sensor	Bands	Wavelength Range	Spatial Resolution	Breadth
GF-5	330	400 nm - 2500 nm	30 m	60 km
EMIT	285	380 nm - 2500 nm	60 m	120 km

3.2. Image Data Processing

Image data processing includes several steps such as image denoising, radiometric calibration, atmospheric correction, and orthorectification.

Hyperspectral image often exhibits minor stripe noise and random noise due to variations in sensor sensitivity, operating conditions (such as radiation and temperature), and changes in the received energy. To improve the image quality of GF-5 data, it is necessary to perform data denoising, which consists of two parts: spatial denoising and spectral denoising. In this paper, the global linear stretching method and the Butterworth filtering method were used for spatial denoising and spectral denoising, respectively. The result was shown in Figure 4.

The EMIT image provides reflectance data with high quality, which means that no pre-processing is required for the data.

3.3. Mineral Mapping Methods

The mapping method used in this paper is based on the Tetracorder mineral mapping algorithm and identification rules developed by the USGS [21]. This method has been successfully applied in mineral mapping conducted by the USGS in areas such as Afghanistan and Australia. We referenced some of the optimization work done by Kaley *et al.* on Tetracorder and implemented the algorithm with Python programming, which supports batch processing, spectral resampling, mineral identification, calculation of absorption peak position shift, and absorption depth. These functions could help in accurately determining the compositions of minerals and aid in filtering and identifying significant mineral abundance. The mapping method can be mainly divided into the following steps: spectral continuum removal, spectral resampling, mineral spectral match, and mineral identification.

Continuum removal involves normalizing the spectrum to remove the effects of the overall reflectance level, thereby enhancing the features related to absorption bands. This step helps in standardizing the spectral signatures, making it easier to compare and analyze the absorption characteristics of different materials. Different from the common practice, this method uses "spectral interval" instead of "endpoints" for continuum removal. As a simple example shown in **Figure 5**, the average wavelength and reflectance values between points A and B are calculated as the left endpoint of the dolomite spectra continuum removal, and similarly, the average between points C and D for the right endpoint. The interval from A to B includes four data points, which helps to reduce the impact of noise and outliers on the continuum removal results.

This paper used the USGS digital spectral library as the source of standard mineral spectral data. Since the standard spectra obtained in the spectral library have different channels and spectral response functions from the spectra of remote sensing images, spectral resampling is required before spectra matching between the image spectra and standard spectra. A spectral convolution resampling method that uses a Gaussian function to model the spectral response function was used to resample the data by calculating the integral differences between different functions [22].

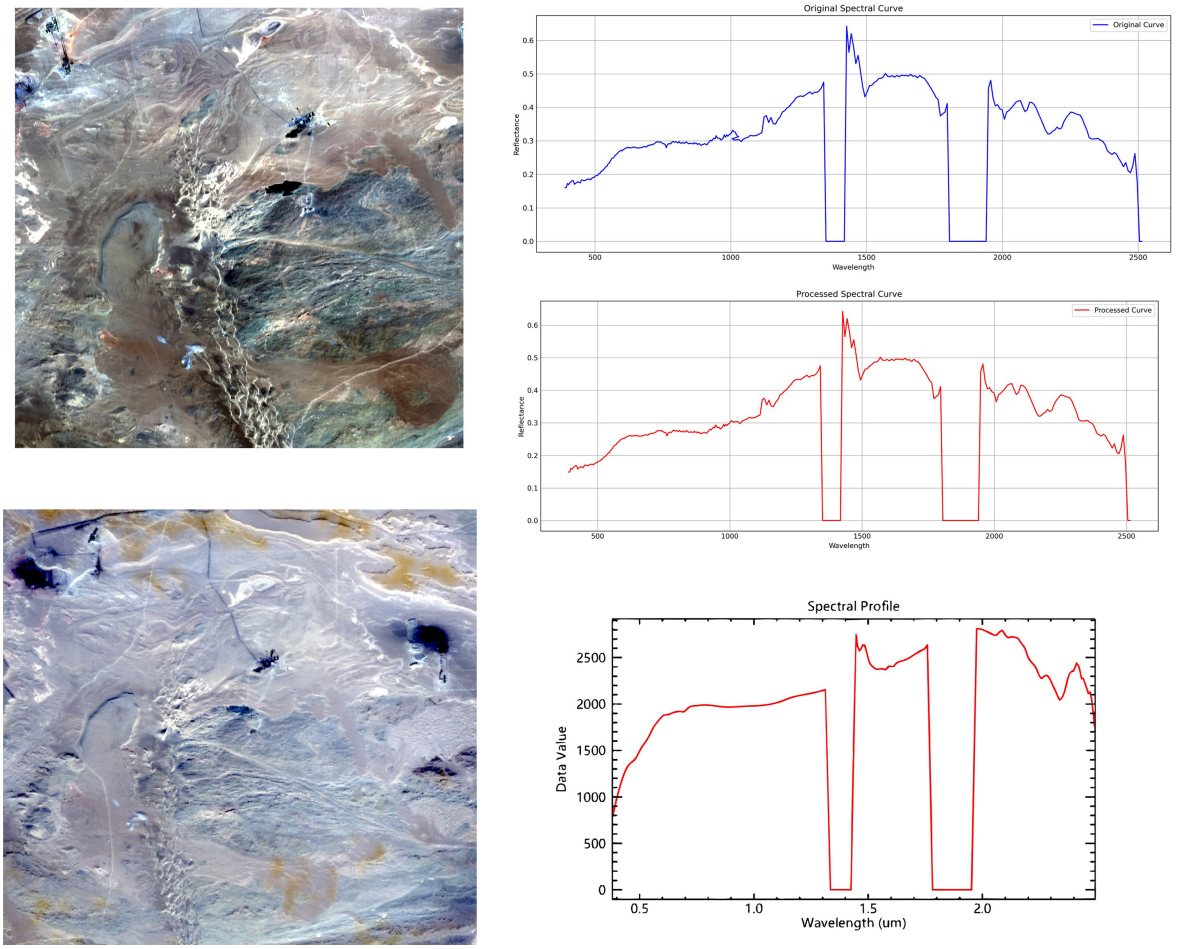

Figure 4. Data processing result of GF-5 and EMIT.

Mineral spectral match and mineral identification are based on the data that has been processed by continuum removal and spectral resampling. Each image pixel spectrum was compared to the standard spectra in the spectral library, and the coefficient of determination (R^2) was calculated as the fitting parameter (F). For minerals that have multiple diagnostic features, "discriminant features" are used to distinguish and identify these minerals. For example, the absorption feature of montmorillonite is centered at 2200 nm, and it has a discriminant feature at 2340 nm. When an image spectrum of muscovite, which shows both the 2200 nm and 2340 nm absorption features, is compared to the standard spectra, the presence of the discriminant feature at 2340 nm ensures that the spectrum is not misidentified as montmorillonite, even if the fit parameter at 2200 nm is very high. The spectra of hyperspectral image pixels are often a mixture of multiple minerals. Given that the USGS standard spectral library includes standard spectra for mixed minerals, the mixed minerals in the image can be identified and classified as distinct categories. The ratio of absorption depths (Dw) between the spectral absorption features of image pixel spectra and those of standard spectra is calculated to indicate the relative abundance of minerals. This step was illustrated in Figure 6.

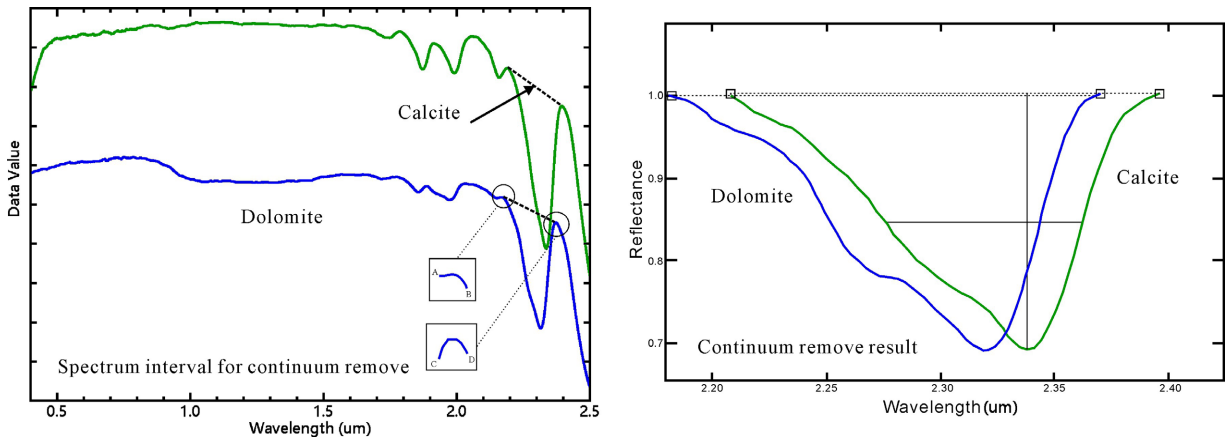

Figure 5. Spectra continuum removal (Left: Calculate the average of the selected endpoints for continuum removal; Right: Spectral curve after continuum removal).

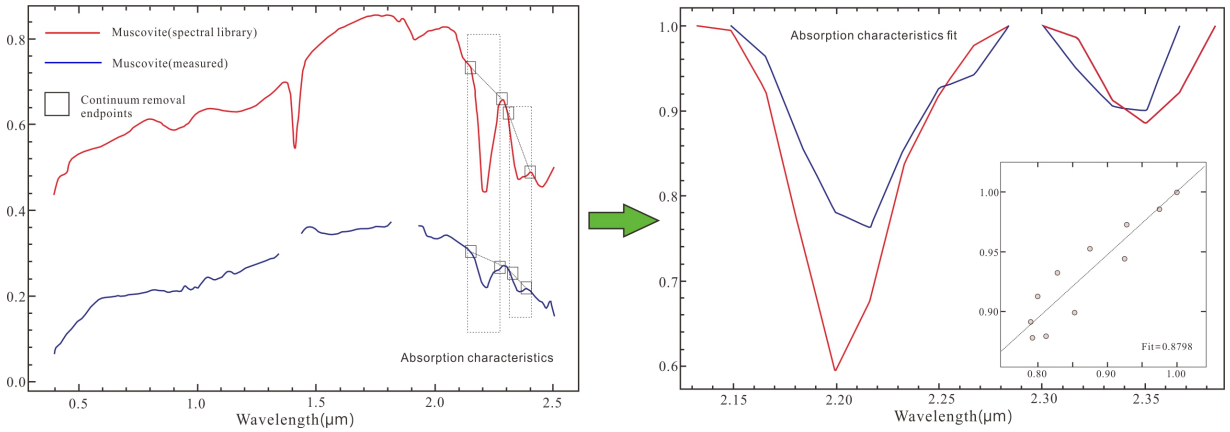

Figure 6. Spectral matching and mineral identification.

The relationship between aluminum content and spectral characteristics of muscovite from the USGS spectral library is shown in Figure 7. The position of the muscovite 2200 nm absorption feature is strongly correlated with its aluminum (Al) content. Therefore, the relative aluminum content in muscovite can be indicated by the 2200 nm absorption peak position [23].

The shift in the spectral absorption feature of sericite is determined by calculating the difference in wavelengths corresponding to the positions of maximum absorption depth. The relative abundance of minerals can be obtained by calculating the absorption depth. The process was shown in Figure 8.

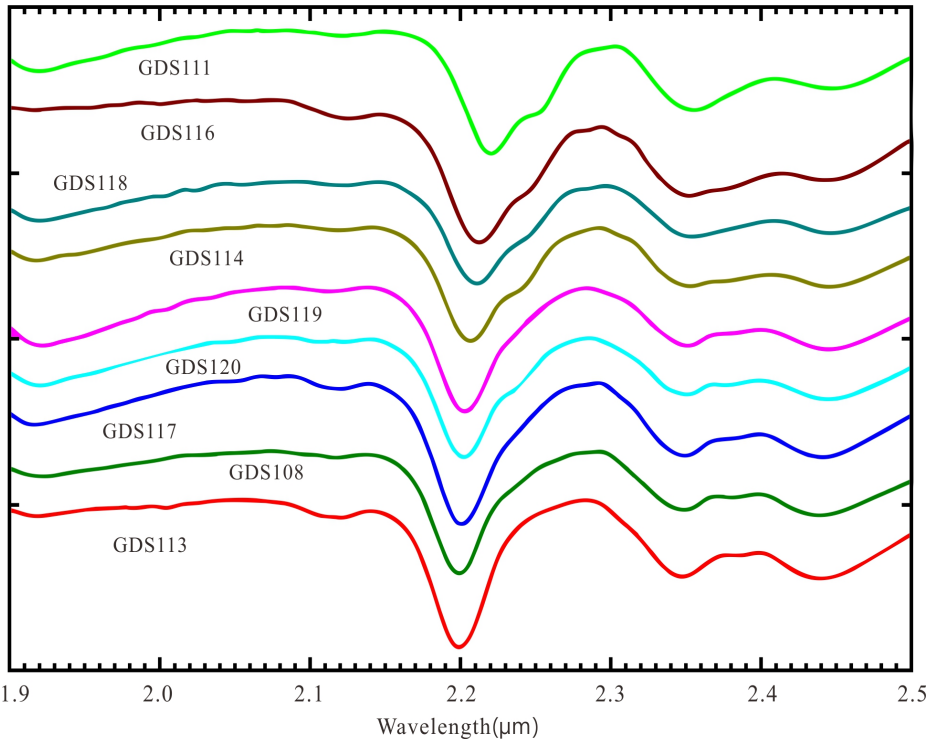

Figure 7. The relationship between absorption wavelength shift and Al content of sericite.

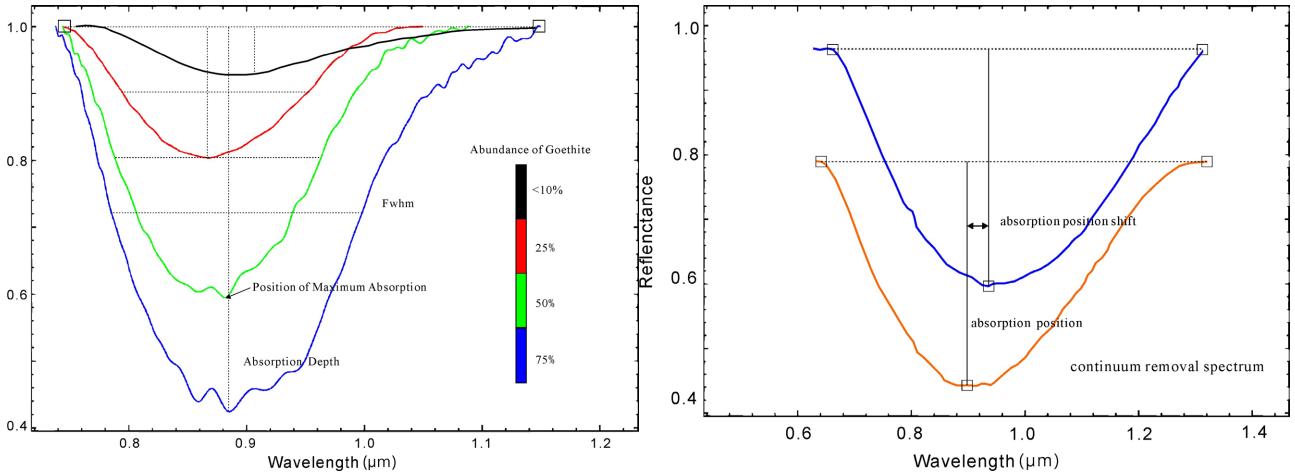

Figure 8. The calculationg method of absorption peak position shift and absorption depth.

The exchange of iron (Fe) and magnesium (Mg) often take place in chlorite, resulting in a variety of compositions. The spectral data from the USGS spectral library in Figure 9 shows that the absorption peak position of chlorite is strongly correlated with the ratio of magnesium to iron content [24]. The calculation method of the chlorite absorption feature shift is the same as that of muscovite.

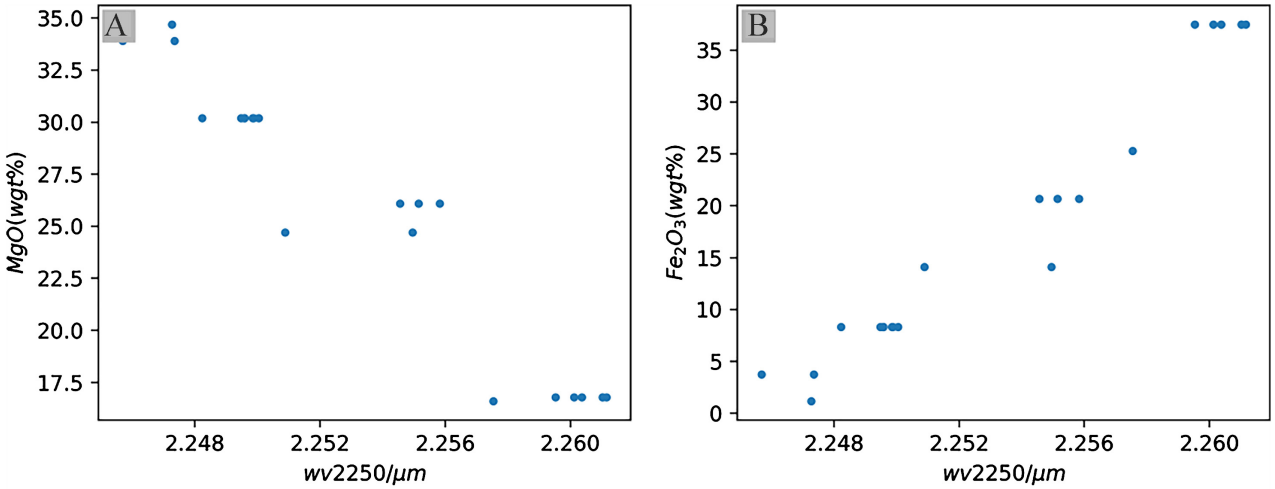

Figure 9. The wavelength of the peak position in chlorite.

4. Results

4.1. Alteration Minerals Mapping

4.1.1. Spectral Characteristics and Distribution of Alteration Minerals

Alteration minerals such as pyrophyllite, alunite, kaolinite, montmorillonite, sericite, chlorite, and calcite were mapped in the Bijia Mountain deposit based on the spectral diagnostic features formed by different mineral functional groups and cations.

The spectral diagnostic features of these altered minerals were shown in Figure 10. Kaolinite and montmorillonite have absorption features at 2200 nm; the difference lies in the fact that montmorillonite's absorption feature is sharper, while kaolinite has a weak feature at a slightly shorter wavelength near 2200 nm. Pyrophyllite was identified based on a sharp diagnostic absorption feature at 2165 nm and another feature at 2320 nm. Alunite has two absorption features in the Atmosphere window at 2190 nm and 2320 nm, which are flatter than the features of pyrophyllite. In addition, alunite and pyrophyllite have a secondary feature at 2210 nm within their primary absorption feature, which is crucial for the identification of the two minerals. Chlorite and calcite have absorption features at 2250 nm and 2340 nm, respectively. Notably, the spectral characteristics of chlorite and epidote are difficult to distinguish in the image, which means that the chlorite identification results in this paper may include epidote.

The distribution of alteration minerals in the Bijia Mountain mining area is shown in Figure 11. Due to the low spatial resolution of images, these minerals are often identified by mixed spectra. Both of the mapping results of EMIT and

GF5 identified alunite, pyrophyllite, and pyrophyllite + kaolinite in the mining area. Alunite and pyrophyllite, visible in only a few pixels in a small area, were concentrated in the center of the mapping area, which was surrounded by a mixture of kaolinite and pyrophyllite. The propylitic zone, primarily composed of chlorite, calcite, and albite, commonly occurs at the periphery of the epithermal system. Therefore, the chlorite + calcite areas identified in this study may indicate the location of the propylitic zone. As shown in Figure 11, the altered minerals in the mining area were distributed along an EW trending that is closely related to the fault in this area. In the central region of the ore body, alunite, kaolinite, and pyrophyllite were identified. The transition zone mainly consisted of sericite and montmorillonite, while the propylitic zone was composed of calcite and chlorite.

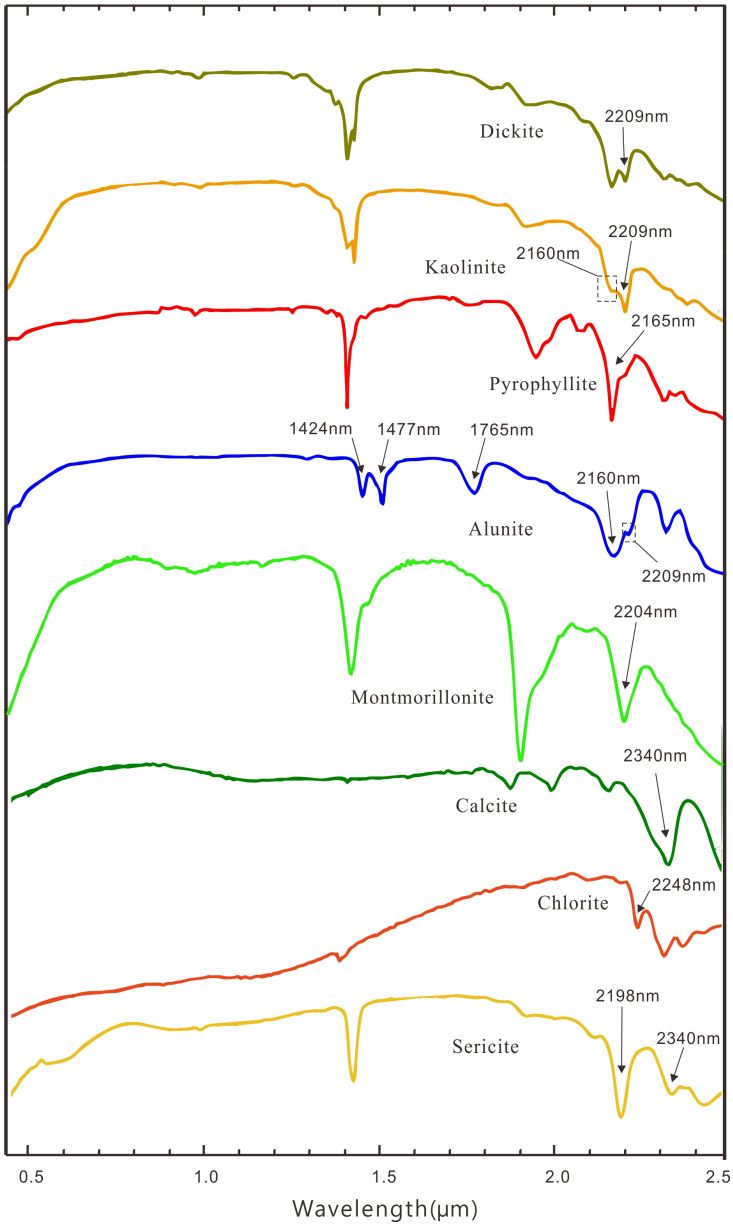

Figure 10. The spectral features of alteration minerals in the Bijia Mountain deposit.

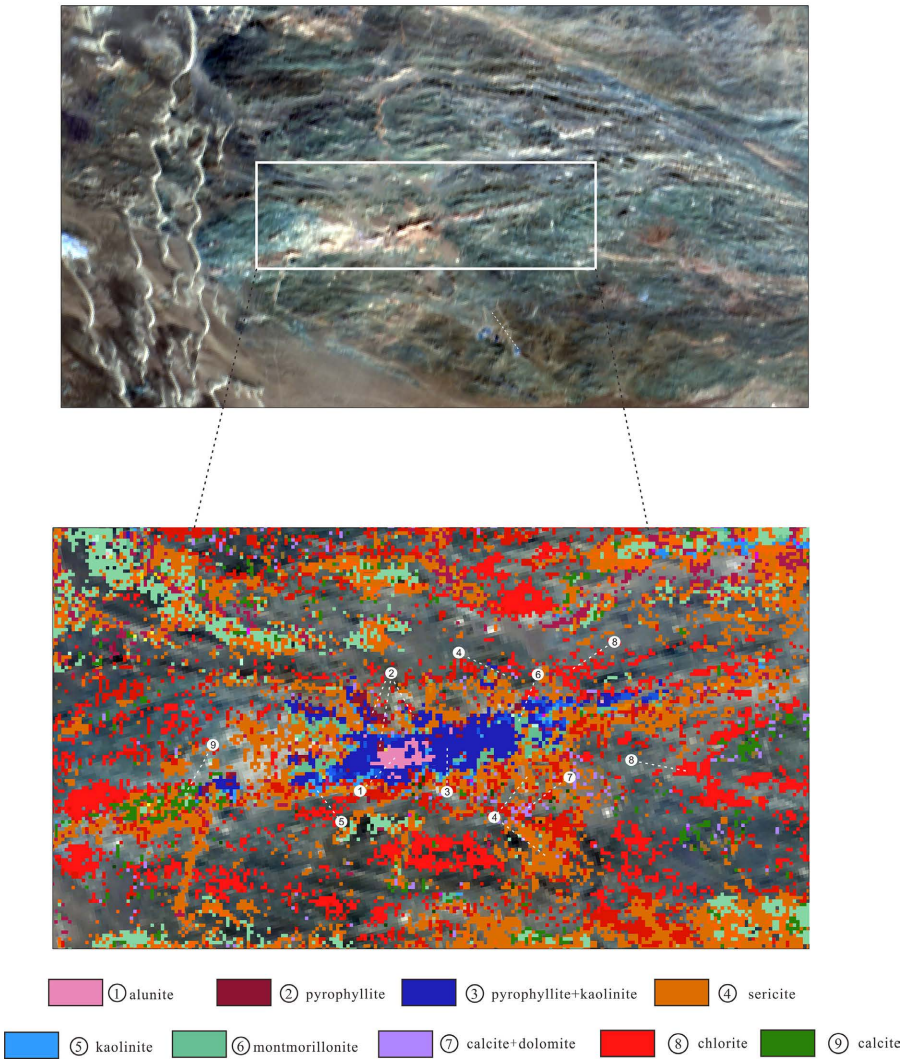

Figure 11. Mineral mapping results in the Bijia Mountain mine area.

To verify the remote sensing mapping results, four groups of rock samples were collected from the ore body and host rocks that had intensive alteration. Their spectra were measured by a spectrometer and compared with the standard spectra to identify the minerals (**Figure 12**).

The spectra analysis result showed the samples were primarily containing kaolinite, alunite, sericite, and montmorillonite, which could demonstrate the accuracy of the mineral mapping result.

4.1.2. Spectral Characteristics and Distribution of Sericite and Chlorite

Sericite is an important mineral for tracing ore-forming hydrothermal fluids. The aluminum (Al), iron (Fe), and silicon (Si) could exchange in the silica-oxygen tetrahedron of sericite, leading to the formation of various aluminum contents of sericite in different fluid conditions [25]. Due to the tetrahedral substitution of aluminum and silicon in sericite, the absorption peak position of Al-OH can shift within 2190 nm to 2228 nm, corresponding to exchange between the aluminum and silicon in

sericite. For aluminum-rich sericite, the absorption feature is typically less than 2195 nm. The absorption peak position for common sericite is between 2200 nm and 2208 nm, while for low-aluminum sericite (with an Si/Al ratio > 3), the absorption peak position is between 2216 nm and 2228 nm. As shown in Figure 13, sericite was distributed along the EW trend faults on the eastern side of the mining area. Compared to the sericite in the periphery area, the absorption features of sericite in the mining area moved towards shorter wavelengths (2198 nm), which means medium aluminum (Al) content. This result indicates that there is a close relationship between the med aluminum (Al) content of sericite and the mineralized zone.

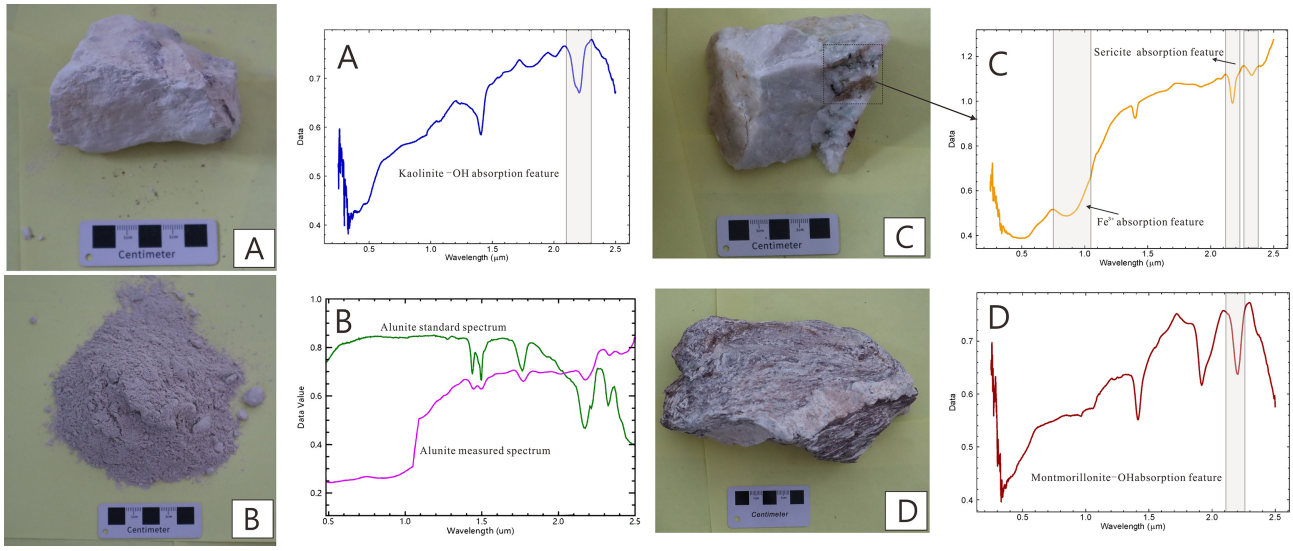

Figure 12. Measured spectra in the Bijia Mountain mine area.

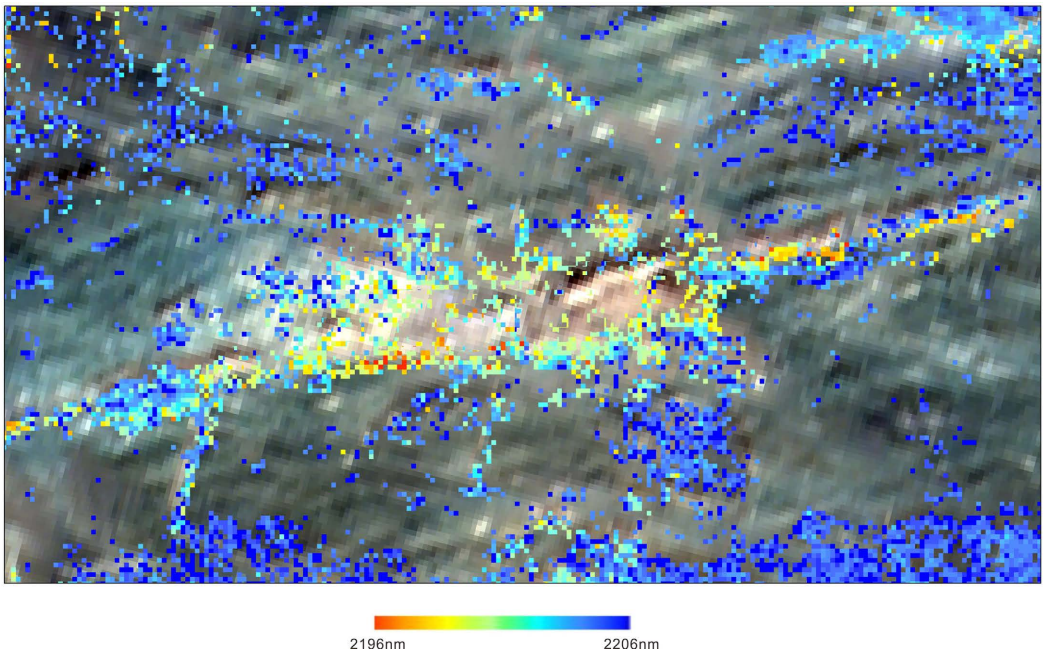

Figure 13. The Al-OH absorption peak shift of sericite in the Bijia Mountain deposit.

Figure 14 shows the spatial distribution of chlorite with different magnesium contents in the mining area. With an increase in the relative magnesium (Mg) content, the absorption peak of chlorite shifts toward shorter wavelengths. The results show that most chlorite in the mapping area does not exhibit a significant tendency toward iron (Fe) or magnesium (Mg) enrichment. Chlorite with Mg-enriched characteristics is predominantly distributed along the edge of the mining area and on the eastern and western sides of the mineralized alteration zone, whereas a bit of chlorite located in the periphery of the orebody displays Fe-enriched characteristics. Overall, the mapping results suggested that the absorption features of chlorite moved towards shorter wavelengths as chlorite got closer to the ore body.

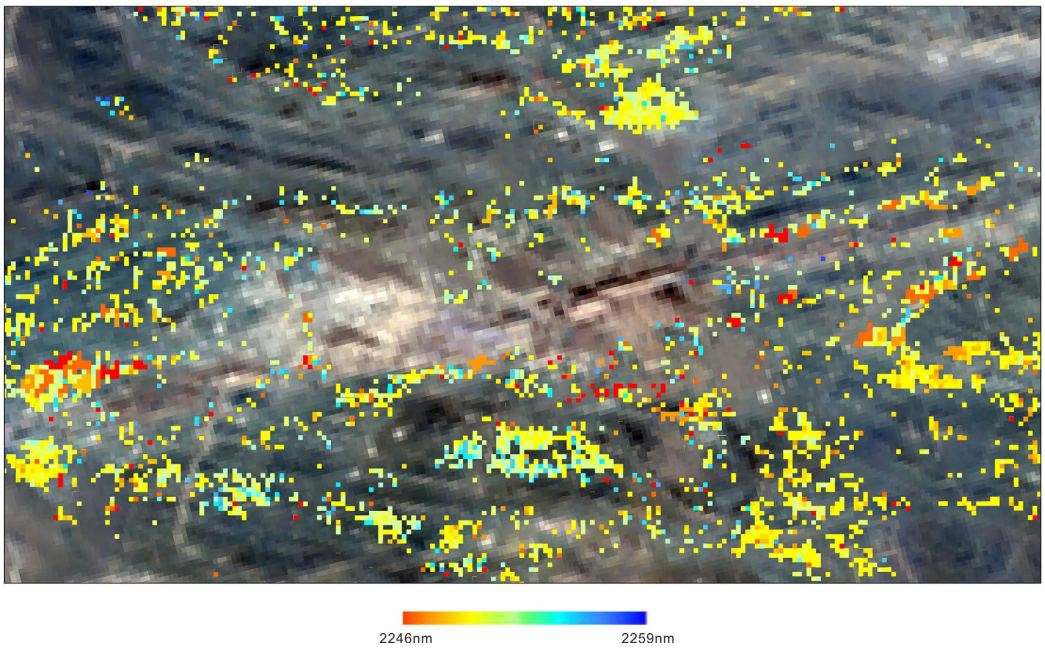

Figure 14. The absorption peak shift of chlorite in the Bijia Mountain deposit.

4.1.3. Spectral Characteristics and Distribution of Iron-Bearing Minerals

It is difficult to identify pyrite in imagery using near-infrared and short-wave infrared (NIR-SWIR) spectroscopy; the iron-bearing minerals identified in this study are primarily limonite. Due to the effect of noise in the 900 - 1100 nm near-infrared band of GF-5 data, the iron-bearing minerals are identified using EMIT data.

Original mineral pyrite in the Bijia Mountain deposit underwent oxidation on the surface, leading to the formation of limonite under relatively neutral conditions. This process results in limonitization, which serves as a significant surface alteration indicator. The relative abundance of ferric iron (Fe^{3+}), derived from absorption depth analysis, indicates that limonitization mainly occurs at the center of the mining area and is spatially associated with minerals such as alunite and kaolinite (Figure 15). Minor occurrences of limonite with sericite and chlorite are found at the edge of the mining area. The mapping results indicate that the abundance and spatial distribution of limonite are closely associated with mineralization.

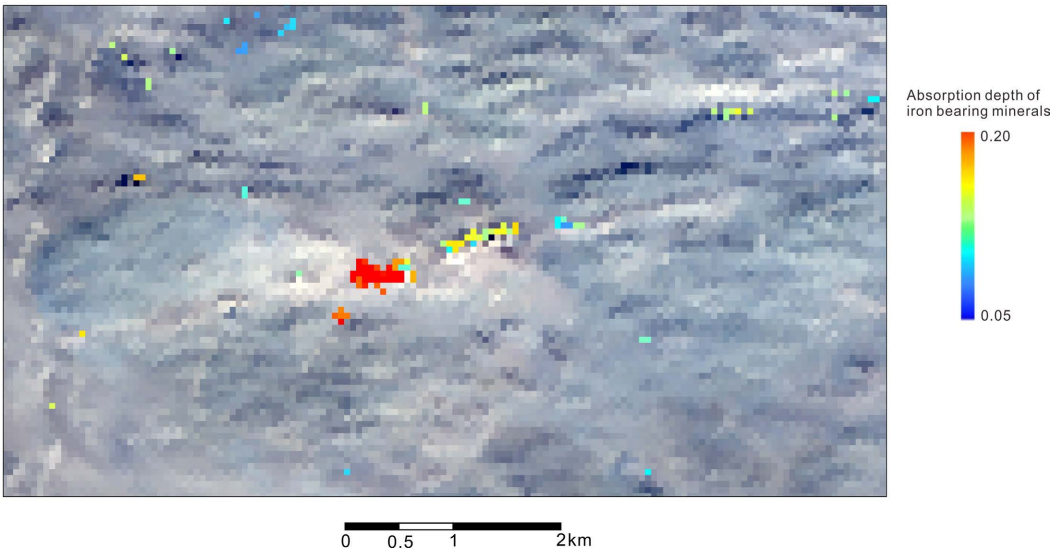

Figure 15. The absorption depth of iron-bearing minerals in the Bijia Mountain deposit.

4.2. Core Spectrum Analysis Result

Some studies indicated that high sulphur epithermal deposits are the shallow occurrence of porphyry hydrothermal systems, and they form a complete volcanic metallogenic series [26] [27]. One of the typical ore-forming model theories suggests that hydrothermal fluids with gold migrate upward from the bottom at low temperature (<300˚C) and form a boiling interface. The fluids migrate through channels with sericite and pyrite in structure fractured zones, and the precious metal deposit with argillic alteration zones was formed in a funnel-shaped tectonic system above the boiling interface [28] [29]. According to such research, the vertical alteration zones and minerals in the ore body profiles can indicate the migrating channels of uplifting thermal fluid, which can provide favorable evidence for epithermal deposits prospecting [30] [31].

This paper analyzed spectral features on core samples of a 160-meter-deep drill, which was located on the EW-trending fault in the central region of the ore body with advanced argillic alteration on the surface (**Figure 16**). The alteration minerals in core samples at depths of 40 m to 160 m in the mining area were identified with a field spectrometer. The mineral identification results show that the altered minerals in the core samples mainly consist of kaolinite, sericite, chlorite, alunite, and pyrophyllite. Alunite, pyrophyllite, and kaolinite were widely distributed in samples at depths less than 100 meters, while samples in 100 to 160 meters contain sericite with minor amounts of chlorite (**Figure 17**). Different from the alteration zones at the surface, alteration minerals at depth lack carbonate minerals, and the chlorite is more iron-enriched, which may be related to the reducing environment and the low temperature of the fluids as they migrate to the surface. The spectral features of argillic alteration minerals and iron in core samples suggest that the drilling locations may be related to the migration channels of ore-bearing hydrothermal fluids.

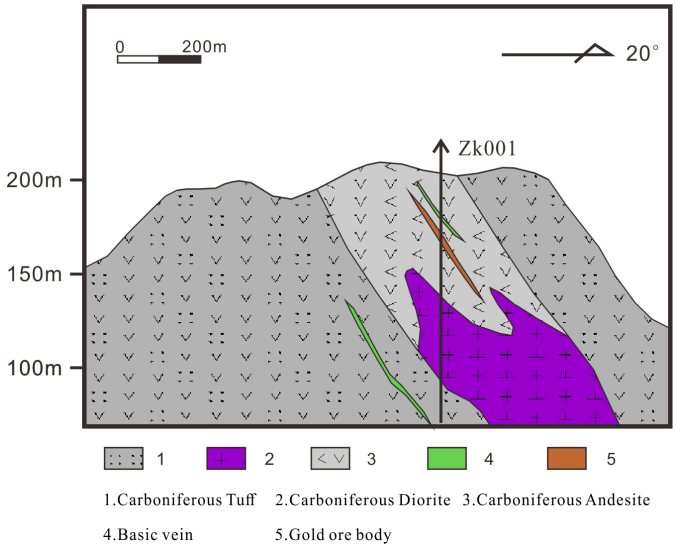

Figure 16. The geological position of core samples.

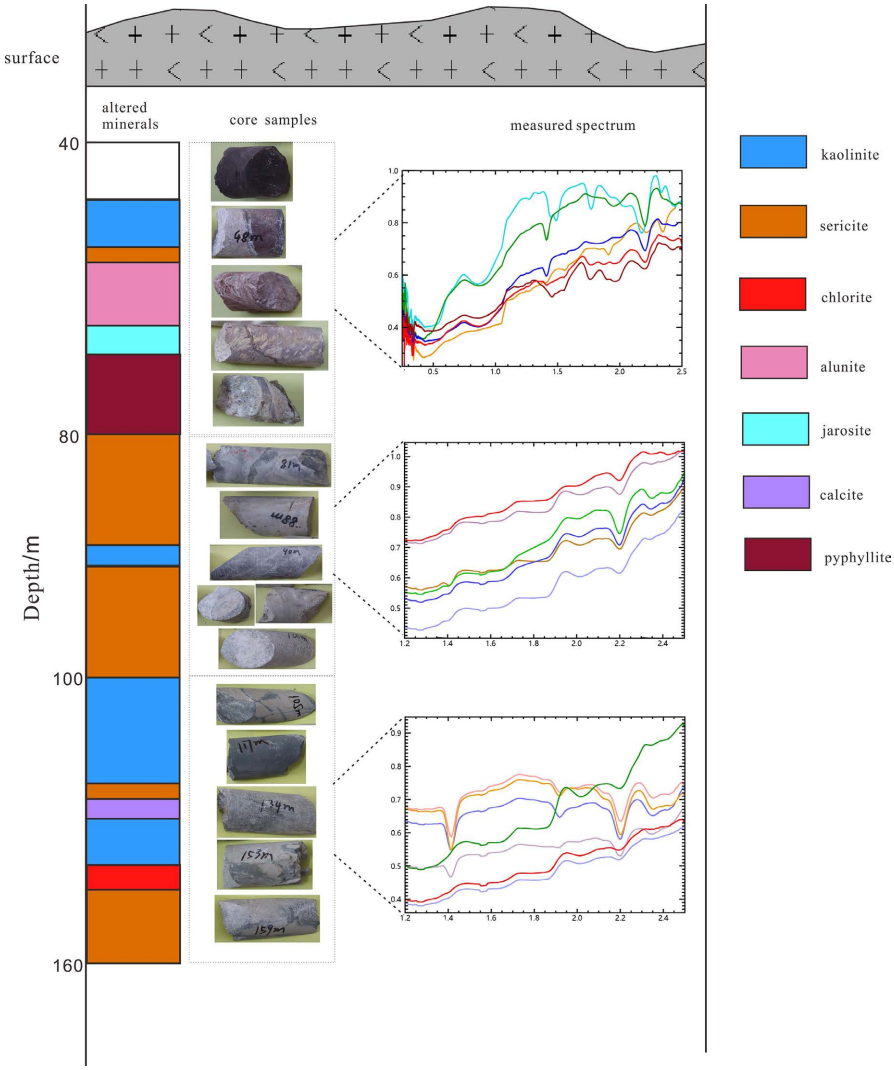

Figure 17. The spectrum of core samples.

5. Discussion

5.1. The Mineral Composition and Indication of Mineralization

In epithermal deposits, the aluminum content of sericite is closely correlated with the alteration zone. The aluminum (Al), iron (Fe), and silicon (Si) could exchange in the silica-oxygen tetrahedron of sericite, leading to the formation of various aluminum contents of sericite in different fluid conditions.

$$\begin{aligned} &2KAl_2\left(AlSi_3\right)O_{10}\left(OH\right)_2\left(sericite^{high-Al}\right)+K^+ +1.5Fe^{2+}+4.5SiO_2+3H_2O \\ &\Leftrightarrow 3KFe_{0.5}Al_{1.5}\left(Al_{0.5}Si_{3.5}\right)O_{10}\left(OH\right)_2\left(sericite^{low-Al}\right)+4H^+ \end{aligned} \quad (1)$$

During the early stage of mineralization, high-temperature, potassium-rich, and near-neutral magmatic fluids favor the formation of aluminum-rich sericite, which is indicative of a heat source and proximity of the mineralization center [32]. As the fluid cools and undergoes water-rock interaction with the host rocks, the pH decreases and aluminum activity declines, resulting in the formation of sericite with low aluminum content. Therefore, variations in aluminum content serve as an indicator for the transition of the hydrothermal fluid from the early mineralization stage to later-stage alteration [33].

This paper extracted the shift in the 2200 nm absorption feature of sericite to illustrate the variations in aluminum content of the sericite in the mining area.

According to **Figure 18**, high-aluminum sericite (absorption peak < 2196 nm) is absent in the Bijia Mountain gold deposit, where the sericite is predominantly of medium-aluminum to low-aluminum composition. Medium-aluminum sericite is distributed on the edge of the mineralized center, where it coexists with kaolinite and limonite. The aluminum content of sericite progressively decreases as one gets farther from the orebody. Medium-aluminum content sericite in the mining area indicates a low temperature, neutral to slightly acidic fluid environment, and its formation is closely associated with argillic alteration zones [34]. Variations in sericite aluminum content can delineate alteration intensity gradients and predict the location of a potential mineralization center.

During hydrothermal alteration or metamorphic processes, variations in fluid composition, oxygen fugacity, redox conditions, temperature, and pressure induce Mg-Fe isomorphic substitution in chlorite. Some studies have shown that specific element content, such as magnesium (Mg) and titanium (Ti) in propylitic alteration minerals, had a decreasing trend from the ore-forming rock body to the periphery area of the mineral deposit, making its Mg/Fe ratio a sensitive indicator of the hydrothermal mineralization environment [35]-[37].

$$\begin{aligned} &2\left(Mg\right)_5Al\left(AlSi_3\right)O_{10}\left(OH\right)_8+12H^+ \Leftrightarrow 4SiO_2+10H_2O+6Mg^{2+}+ \\ &\left(Mg_4Al\right)Al\left(Al_2Si_2\right)O_{10}\left(OH\right)_8 \end{aligned} \quad (2)$$

The magnesium (Mg) content of chlorite can be described by the shift in the 2250 nm absorption peak. The variation of the chlorite 2250 nm absorption peak within the mining area is shown in **Figure 19**, which reflects the changes in the relative contents of magnesium (Mg) and iron (Fe) in chlorite.

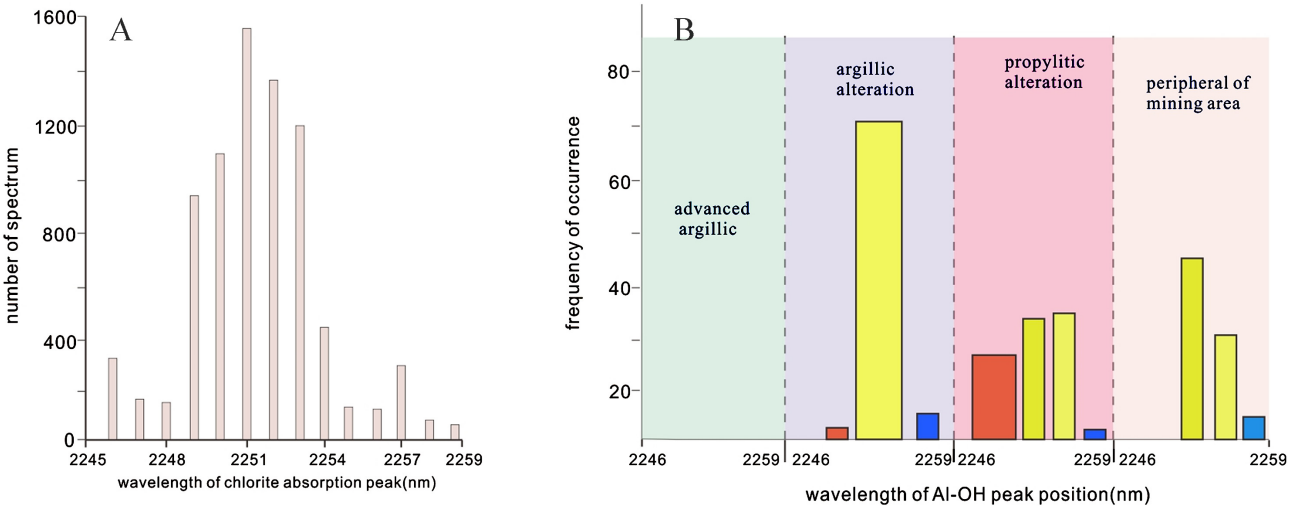

Figure 18. The absorption peak of sericite in the Bijia Mountain deposit. (A) The number of pixels with a different absorption peak of sericite; (B) The percentage of various types of sericite in different alteration zones.

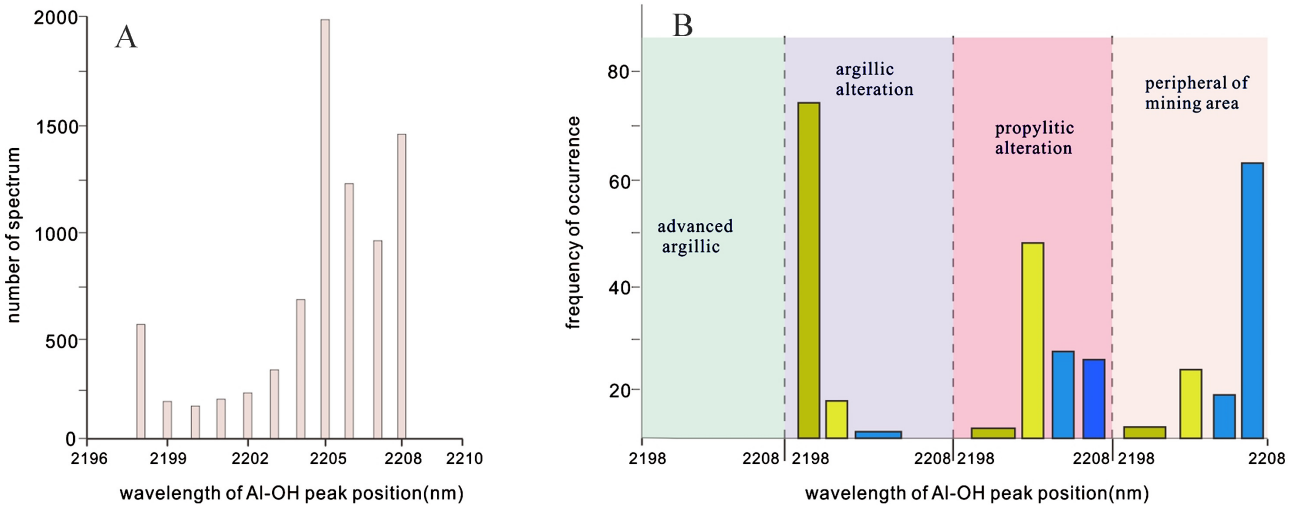

Figure 19. The absorption peak of chlorite in the Bijia Mountain deposit. (A) The number of pixels with a different absorption peak of chlorite; (B) The percentage of various types of chlorite in different alteration zones.

In the vertical profile, chlorite in core samples of the Bijia Mountain gold deposit exhibits iron-enriched characteristics, whereas surface chlorite is more magnesium-enriched and spatially coincides with areas containing limonite. The Mg/Fe content variation trend of chlorite and the degree of limonitization may reflect the redox conditions during different stages of mineralization, indicating the hydrothermal fluid pathways from depth toward the surface and the associated changes in mineralization conditions with depth: Under the relatively reducing conditions at depth, iron may exist in the divalent state (Fe^{2+}) and participate in the formation of iron-rich chlorite. In contrast, under the oxidizing conditions at the surface, Fe^{2+} is oxidized to the trivalent state (Fe^{3+}), which favors the formation of limonite and magnesium-rich chlorite.

On the surface of the mining area, iron-enriched chlorite occurs predominantly

in the periphery, whereas chlorite within the central part of the mine is relatively more magnesium-enriched. A possible explanation is that chlorite from these two distinct locations formed under different geological environments. Chlorite occurring outside the mining area likely precipitated in a shallow marine sedimentary environment, with iron sourced from marine sediments. In contrast, the magnesium-rich chlorite within the mineralized alteration zone primarily formed during hydrothermal activity. This distinction means chlorite with high magnesium (Mg) content can serve as an indicator for locating the ore body.

5.2. Alteration Zones for Mineral Prospecting

Based on the alteration mineral assemblages in the Bijia Mountain gold deposit, the alteration zones on the surface could be identified mainly into three parts (Figure 20). The advanced argillic zone located at the center of the orebody was primarily composed of pyrophyllite, alunite, limonite, and kaolinite. The argillic zone, transition from the centre of the ore body to the edge, mainly consisted of medium aluminum content sericite, kaolinite, and montmorillonite. The propylitic zone was located at the edge of the mining area and was composed of magnesium-rich chlorite and a minor amount of calcite.

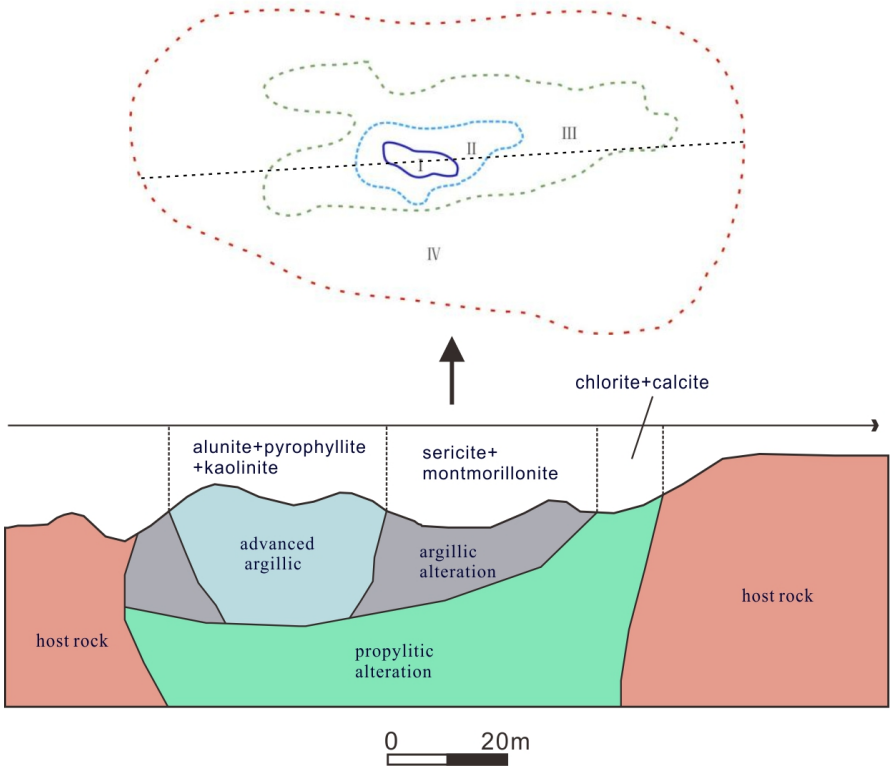

Figure 20. The alteration zone indicates mineralization in the Bijia Mountain deposit.

The hydrothermal alteration zoning observed at the surface indicates the presence of a phyllic cap composed of pyrophyllite, alunite, and kaolinite in the shal-

low portion of the Bijia Mountain gold deposit, marking the center of past volcanic hydrothermal activity. The advanced argillic zone is closely associated with east-west trending structures, suggesting the existence of a low-pressure alteration zone. The medium aluminum sericite occurs adjacent to the center of the orebody and constitutes a key mineral component of the transitional zone within the argillic alteration assemblage. The coexistence of chlorite and calcite at the margin of the mining area reflects a medium- to low-temperature, CO_2-rich hydrothermal environment, characteristic of typical distal alteration. The assemblage and compositional variations of alteration minerals in the Bijia Mountain mining area reflect two distinct mineralization stages—hydrothermal ore-forming and supergene oxidation, which could serve as a key indicator for locating orebodies with remote sensing data.

6. Conclusions

This study mapped minerals in the Bijia Mountain deposit using the GeoAHSI mapping tool with GF-5 and EMIT hyperspectral data. The mapping results extracted the spatial distributions of minerals such as kaolinite, chlorite, sericite, limonite, alunite, pyrophyllite, and montmorillonite. The advanced argillic zone, argillic transition zone, and propylitic zone were delineated based on surface mineral assemblages. This indicates that GF-5 and EMIT hyperspectral data can be used to locate small-scale epithermal ore bodies.

This paper distinguishes between chlorite and sericite located in the periphery and inside parts of the ore district based on their spectral characteristics. On the surface of the mining area, chlorite and sericite exhibit trends of magnesium (Mg) enrichment and aluminum (Al) enrichment as they get closer to the ore body. Fe-rich chlorite at depth, pyrophyllite and alunite associated with the mineralization center may correspond to the hydrothermal mineralization stage of the Bijia Mountain gold deposit, whereas kaolinite, limonite, and Mg-rich chlorite on the surface may be related to the late mineralization and supergene oxidation stages. Advanced argillic minerals (pyrophyllite + kaolinite), medium-aluminum sericite, and Mg-rich chlorite can serve as remote sensing prospecting indicators for the Bijia Mountain gold deposit. This research could provide a valuable case study for epithermal deposit prospecting in the arc belt.

Funding

This research was funded by "Study on Kiwifruit Monitoring Model in the Western Guanzhong Basin Based on Hyperspectral Remote Sensing Technology (No. 2024JC-YBQN-0318)" and "Science and Technology Innovation Foundation of Comprehensive Survey & Command Center for Natural Resources (Program No. KC20240009)".

Conflicts of Interest

The authors declare no conflicts of interest regarding the publication of this paper.

References

[1] Mao, X., Chen, Y., Liu, Z., Yang, X., Li, S., Wang, D., *et al.* (2024) Hydrothermal Alteration and Its Geochemistry of the Xiadian Gold Deposit, Jiaodong Peninsula, China: Implications for Fluid-Rock Interaction Processes and Mineral Exploration. *Ore Geology Reviews*, **170**, Article 106134. https://doi.org/10.1016/j.oregeorev.2024.106134

[2] Ghasemi Siani, M. and Lentz, D.R. (2022) Lithogeochemistry of Various Hydrothermal Alteration Types Associated with Precious and Base Metal Epithermal Deposits in the Tarom-Hashtjin Metallogenic Province, NW Iran: Implications for Regional Exploration. *Journal of Geochemical Exploration*, **232**, Article 106903. https://doi.org/10.1016/j.gexplo.2021.106903

[3] Kopačková, V. and Koucká, L. (2017) Integration of Absorption Feature Information from Visible to Longwave Infrared Spectral Ranges for Mineral Mapping. *Remote Sensing*, **9**, Article 1006. https://doi.org/10.3390/rs9101006

[4] Yuan, C., Zhao, J., Liu, Z., Liu, X. and Tang, J. (2025) Detecting Mineralization via White Mica Spectral Footprints: From Field-Based Sampling to Satellite Hyperspectral Remote Sensing. *Ore Geology Reviews*, **181**, Article 106588. https://doi.org/10.1016/j.oregeorev.2025.106588

[5] Zhai, S., Jian, W., Mao, J., Duan, S., Zuo, J. and Sun, P. (2023) Significance of Pyrophyllite Parameters in Shortwave Infrared Spectroscopy: A Case Study of the Guihu Super-Large Pyrophyllite Deposit. *Ore Geology Reviews*, **155**, Article 105374. https://doi.org/10.1016/j.oregeorev.2023.105374

[6] Portela, B., Sepp, M.D., van Ruitenbeek, F.J.A., Hecker, C. and Dilles, J.H. (2021) Using Hyperspectral Imagery for Identification of Pyrophyllite-Muscovite Intergrowths and Alunite in the Shallow Epithermal Environment of the Yerington Porphyry Copper District. *Ore Geology Reviews*, **131**, Article 104012. https://doi.org/10.1016/j.oregeorev.2021.104012

[7] Cooke, D.R. and Simmons, S.F. (2000) Characteristics and Genesis of Epithermal Gold Deposits. *Reviews in Economic Geology*, **13**, 221-244.

[8] Corrado, F., Putzolu, F., Armstrong, R.N., Mondillo, N., Chirico, R., Casarotto, B., *et al.* (2025) Application of Satellite and Proximal Hyperspectral Sensing to Target Lithium Mineralization in Volcano-Sedimentary Deposits: A Case Study from the McDermitt Caldera, USA. *Remote Sensing of Environment*, **323**, Article 114724. https://doi.org/10.1016/j.rse.2025.114724

[9] Zhou, Y., Chen, S., Li, L., Fan, F., Zhang, H., Chen, J., *et al.* (2023) Mapping Hydrothermal Alteration of the Au-Cu Deposits in the Zhenghe Magmatic-Hydrothermal Mineralization System, SE China, Using Short Wavelength Infrared (SWIR) Reflectance Spectroscopy. *Journal of Geochemical Exploration*, **244**, Article 107113. https://doi.org/10.1016/j.gexplo.2022.107113

[10] Lorenz, S., Ghamisi, P., Kirsch, M., Jackisch, R., Rasti, B. and Gloaguen, R. (2021) Feature Extraction for Hyperspectral Mineral Domain Mapping: A Test of Conventional and Innovative Methods. *Remote Sensing of Environment*, **252**, Article 112129. https://doi.org/10.1016/j.rse.2020.112129

[11] Jain, R. and Bhu, H. (2024) Potentials of Spaceborne Imaging Spectrometer PRISMA, ASTER, and ALOS-1 PALSAR Datasets for Mineral Mapping and Geological Controls of Mineral Deposit in Jahazpur, Rajasthan, India. *Remote Sensing Applications: Society and Environment*, **34**, Article 101193. https://doi.org/10.1016/j.rsase.2024.101193

[12] Chen, Q., Zhao, Z., Zhou, J., Zhu, R., Xia, J., Sun, T., *et al.* (2022) ASTER and GF-5

Satellite Data for Mapping Hydrothermal Alteration Minerals in the Longtoushan Pb-Zn Deposit, SW China. *Remote Sensing*, **14**, Article 1253. https://doi.org/10.3390/rs14051253

[13] Habashi, J., Jamshid Moghadam, H., Mohammady Oskouei, M., Pour, A.B. and Hashim, M. (2024) PRISMA Hyperspectral Remote Sensing Data for Mapping Alteration Minerals in Sar-E-Châh-E-Shur Region, Birjand, Iran. *Remote Sensing*, **16**, Article 1277. https://doi.org/10.3390/rs16071277

[14] Huo, H., Ni, Z., Jiang, X., Zhou, P. and Liu, L. (2015) Mineral Mapping and Ore Prospecting with Hymap Data over Eastern Tien Shan, Xinjiang Uyghur Autonomous Region. *Remote Sensing*, **6**, 11829-11851. https://doi.org/10.3390/rs61211829

[15] Jing, M., Jian, Y., Chun, H. and Zhi, W. (2002) Metallogenic Systems of Polymetallic Copper and Gold Deposits and Related Metallogenic Geodynamic Model in Eastern Tianshan, Xinjiang. *Earth Science-Journal of China University of Geosciences*, **27**, 413-424.

[16] Asadzadeh, S., Zhou, X. and Chabrillat, S. (2024) Assessment of the Spaceborne Enmap Hyperspectral Data for Alteration Mineral Mapping: A Case Study of the Reko Diq Porphyry Cu Au Deposit, Pakistan. *Remote Sensing of Environment*, **314**, Article 114389. https://doi.org/10.1016/j.rse.2024.114389

[17] Dong, X., Gan, F., Li, N., Zhang, S. and Li, T. (2022) Mineral Mapping in the Duolong Porphyry and Epithermal Ore District, Tibet, Using the Gaofen-5 Satellite Hyperspectral Remote Sensing Data. *Ore Geology Reviews*, **151**, Article 105222. https://doi.org/10.1016/j.oregeorev.2022.105222

[18] Wang, L., Cao, M.-J., Gao, S., Chiaradia, M., Hollings, P., Qin, K.Z., *et al.* (2024) The Magmatic Origin of Propylitic Alteration of the Zhengguang Epithermal Au-Zn Deposit, Heilongjiang, China: Evidence from Mineral Compositions and H-O-Sr Isotopes. *Mineralium Deposita*, **59**, 1017-1038. https://doi.org/10.1007/s00126-023-01243-2

[19] Wang, J.B., Wang, Y.W. and He, Z.J. (2006) Ore Deposits as a Guide to the Tectonic Evolution in the East Tianshan Mountains, NW China. *Geology in China*, **33**, 462-469.

[20] Xiao, W.J., Qin, K.Z., Sun, S. and Li, J.L. (2004) Paleozoic Accretionary and Collisional Tectonics of the Eastern Tianshan (China): Implications for the Continental Growth of Central Asia. *American Journal of Science*, **304**, 370-395. https://doi.org/10.2475/ajs.304.4.370

[21] Clark, R.N. and Roush, T.L. (1984) Reflectance Spectroscopy: Quantitative Analysis Techniques for Remote Sensing Applications. *Journal of Geophysical Research*: *Solid Earth*, **89**, 6329-6340. https://doi.org/10.1029/jb089ib07p06329

[22] Swayze, G.A., Clark, R.N., Goetz, A.F.H., Chrien, T.G. and Gorelick, N.S. (2003) Effects of Spectrometer Band Pass, Sampling, and Signal-to-Noise Ratio on Spectral Identification Using the Tetracorder Algorithm. *Journal of Geophysical Research*: *Planets*, **108**, Article No. 5105. https://doi.org/10.1029/2002je001975

[23] Clark, R.N., Swayze, G.A., Livo, K.E., Kokaly, R.F., Sutley, S.J., Dalton, J.B., *et al.* (2003) Imaging Spectroscopy: Earth and Planetary Remote Sensing with the USGS Tetracorder and Expert Systems. *Journal of Geophysical Research*: *Planets*, **108**, 1-44. https://doi.org/10.1029/2002je001847

[24] Kokaly, R.F., Clark, R.N., Swayze, G.A., Livo, K.E., Hoefen, T.M., Pearson, N.C., Wise, R.A., Benzel, W.M., Lowers, H.A., Driscoll, R.L. and Klein, A.J. (2017) USGS Spectroscopic Library Version 7. U.S. Geological Survey Data Series 1035.

[25] Yang, K., Huntington, J.F., Gemmell, J.B. and Scott, K.M. (2011) Variations in Composition and Abundance of White Mica in the Hydrothermal Alteration System at

Hellyer, Tasmania, as Revealed by Infrared Reflectance Spectroscopy. *Journal of Geochemical Exploration*, **108**, 143-156. https://doi.org/10.1016/j.gexplo.2011.01.001

[26] White, N.C. and Hedenquist, J.W. (1990) Epithermal Environments and Styles of Mineralization: Variations and Their Causes, and Guidelines for Exploration. *Journal of Geochemical Exploration*, **36**, 445-474. https://doi.org/10.1016/0375-6742(90)90063-g

[27] Terzi, M.H., Yılmazer, E., Kuşcu, İ., Oyman, T. and Bozan, S. (2024) Mineralogy, Fluid Inclusion and Stable Isotope Characteristics of the Inlice (Konya, Türkiye) High Sulfidation Epithermal Gold Deposit: Implications for Hydrothermal Evolution and Ore Genesis. *Geochemistry*, **84**, Article 126040. https://doi.org/10.1016/j.chemer.2023.126040

[28] Wang, L., Chiaradia, M., Qin, K., Hui, K., Li, Z., Cao, M., *et al.* (2024) Magmatic Controls on Au- and Ag-Rich Intermediate-Sulfidation Epithermal Deposits from Northeast China. *Economic Geology*, **119**, 1913-1936. https://doi.org/10.5382/econgeo.5118

[29] Wilkinson, J.J. (2001) Fluid Inclusions in Hydrothermal Ore Deposits. *Lithos*, **55**, 229-272. https://doi.org/10.1016/s0024-4937(00)00047-5

[30] Cao, M., Hollings, P., Evans, N.J., Cooke, D.R., McInnes, B.I.A., Zhao, K., *et al.* (2020) *In Situ* Elemental and Sr Isotope Characteristics of Magmatic to Hydrothermal Minerals from the Black Mountain Porphyry Deposit, Baguio District, Philippines. *Economic Geology*, **115**, 927-944. https://doi.org/10.5382/econgeo.4701

[31] Audétat, A. (2019) The Metal Content of Magmatic-Hydrothermal Fluids and Its Relationship to Mineralization Potential. *Economic Geology*, **114**, 1033-1056. https://doi.org/10.5382/econgeo.4673

[32] Zhong, J., Chen, Y., Chen, J., Qi, J. and Dai, M. (2018) Geology and Fluid Inclusion Geochemistry of the Zijinshan High-Sulfidation Epithermal Cu-Au Deposit, Fujian Province, SE China: Implication for Deep Exploration Targeting. *Journal of Geochemical Exploration*, **184**, 49-65. https://doi.org/10.1016/j.gexplo.2017.10.004

[33] Meyer, J.M., Kokaly, R.F. and Holley, E. (2022) Hyperspectral Remote Sensing of White Mica: A Review of Imaging and Point-Based Spectrometer Studies for Mineral Resources, with Spectrometer Design Considerations. *Remote Sensing of Environment*, **275**, Article 113000. https://doi.org/10.1016/j.rse.2022.113000

[34] Meyer, J.M., Holley, E.A. and Kokaly, R.F. (2024) Hyperspectral Mapping of Magmatic-Hydrothermal Sericite, Battle Mountain Mining District, Nevada. *Journal of Geochemical Exploration*, **259**, Article 107395. https://doi.org/10.1016/j.gexplo.2024.107395

[35] Wang, L., Qin, K.Z., Song, G.X., Pang, X.Y., Li, G.M. and Zou, X.Y. (2020) Geology and Genesis of the Early Paleozoic Zhengguang Intermediate-Sulfidation Epithermal Au-Zn Deposit, Northeast China. *Ore Geology Reviews*, **124**, Article 103602. https://doi.org/10.1016/j.oregeorev.2020.103602

[36] Lypaczewski, P. and Rivard, B. (2018) Estimating the Mg# and Alvi Content of Biotite and Chlorite from Shortwave Infrared Reflectance Spectroscopy: Predictive Equations and Recommendations for Their Use. *International Journal of Applied Earth Observation and Geoinformation*, **68**, 116-126. https://doi.org/10.1016/j.jag.2018.02.003

[37] Contreras Acosta, I.C., Khodadadzadeh, M. and Gloaguen, R. (2021) Resolution Enhancement for Drill-Core Hyperspectral Mineral Mapping. *Remote Sensing*, **13**, Article 2296. https://doi.org/10.3390/rs13122296